INTERNATIONAL JOURNAL FOR NUMERICAL METHODS IN FLUIDS, VOL. 17, 975–993 (1993)

AN EXPLICIT TRANSIENT ALGORITHM FOR PREDICTING INCOMPRESSIBLE VISCOUS FLOWS IN ARBITRARY GEOMETRY

A. MUKHOPADHYAY, T. SUNDARARAJAN AND G. BISWAS*

Department of Mechanical Engineering, Indian Institute of Technology, Kanpur, U.P. 208016, India

SUMMARY

A numerical method for predicting viscous flows in complex geometries has been presented. Integral mass and momentum conservation equations are deployed and these are discretized into algebraic form through numerical quadrature. The physical domain is divided into a number of non-orthogonal control volumes which are isoparametrically mapped on to standard rectangular cells. Numerical integration for unsteady mementum equations is performed over such non-orthogonal cells. The explicitly advanced velocity components obtained from unsteady momentum equations may not necessarily satisfy the mass conservation condition in each cell. Compliance of the mass conservation equation and the consequent evolution of correct pressure distribution are accomplished through an iterative correction of pressure and velocity till divergence-free condition is obtained in each cell. The algorithm is applied on a few test problems, namely, lid-driven square and oblique cavities, developing flow in a rectangular channel and flow over square and circular cylinders placed in rectangular channels. The results exhibit good accuracy and justify the applicability of the algorithm.

This Explicit Transient Algorithm for Flows in Arbitrary Geometry is given a generic name EXTRA-FLAG.

KEY WORDS Navier–Stokes equations Mass and momentum balance Non-orthogonal control volume Gauss–Legendre quadrature Pressure correction Flow over bluff bodies

1. INTRODUCTION

The solution of full Navier–Stokes equations has been the subject of research for the past few decades. Especially, numerical solution of incompressible viscous flows in terms of primitive variables has posed severe challenges to the researchers. The difficulties mainly arise from the absence of any obvious equation for pressure and the nature of spatial coupling of the pressure and velocity. With the concept of staggered pressure and velocity grids the full Navier–Stokes equations have been solved by finite-difference-based explicit transient algorithms such as MAC[1] and SMAC,[2] where the corrected pressures are obtained from the solution of a Poisson equation. A related technique developed by Chorin[3] involves simultaneous iteration on pressure and velocity to obtain a converged solution. Hirt and Cook[4] have developed a simplified explicit flow solver using the aforesaid pressure–velocity iteration for the solution of a wide variety of problems involving three-dimensional incompressible flows. However, implicit methods are

* Author for correspondence

0271–2091/93/230975–19$14.50

Received January 1993
Revised August 1993

indeed attractive since they do not have stability restrictions on the time steps. The SIMPLE algorithm of Patankar and Spalding[5] provided a successful implicit procedure with primitive variables. The basic SIMPLE algorithm is modified as SIMPLER[6,7] and SIMPLEC[8] for enhanced rate of convergence. The SIMPLE and its variants have dominated over the past decade in the field of numerical modelling of incompressible flows.

In order to extend the application of the above-mentioned flow solvers to complex geometries, non-orthogonal body-conforming co-ordinate systems have been used. Works of Thompson *et al.*,[9] Vanka *et al.*,[10] Raithby *et al.*[11] and Shyy *et al.*[12] may be mentioned in this connection. Peric[13] has attempted to utilize a non-staggered variable arrangement for the calculation of flow in a curved irregular geometry. The difficulty with this approach is that the flow equations in the transformed co-ordinates are always complicated and quite often a multi-block approach seems needful. For flows in complex geometries, the finite element method is attractive due to its geometrically additive property. However, preserving the transportive property of advective terms in the flow equations is non-trivial in finite element method and this aspect requires further research. The application of the finite element method to flow problems has been discussed by Zienkiewicz[14] and Taylor and Hughes.[15] Baliga and Patankar[16] have initiated a finite-element-based control volume method that incorporates some of the key FEM ideas such as non-orthogonal cell geometry, multidirectional interpolation and assembling of elements. Prakash and Patankar[17] have conducted more extensive investigations on this algorithm.

Despite the several stimulating developments as stated above, research is still active on computation of incompressible flows in complex geometries. The common difficulties are the derivation of conservation principles for non-orthogonal control volumes, development of appropriate multidirectional interpolation schemes and the enormity of book keeping for both dependent and independent variables. Here, a novel algorithm (EXTRA-FLAG) using primitive variables is proposed for non-orthogonal geometries which resolves some of the above-mentioned difficulties. Ideas such as element-wise interpolation and transformation of non-orthogonal element geometry into a square computational element have been incorporated while solving the integral conservation equations. The proposed method has been applied to different test problems. These problems include lid-driven square and oblique cavities, developing flow in a two-dimensional rectangular channel and flows over square and circular cylinders in rectangular channels. The method exhibits excellent accuracy and good convergence characteristics.

2. DESCRIPTION OF THE EXTRA-FLAG ALGORITHM

Here the EXTRA-FLAG algorithm is illustrated for the simulation of unsteady incompressible flows in arbitrary shaped two-dimensional geometries.

2.1. Domain discretization and governing equations

The domain is discretized into small curvilinear quadrilateral cells (Figure 1). The velocity nodes are located at the vertices and the pressure nodes are located at the centroids of these cells. The continuity control volumes (CV1) are formed by grid lines connecting velocity nodes. Similarly, momentum control volumes (CV2) are formed by curvilinear quadrilaterals whose vertices are the pressure nodes. However, the velocities for any point within CV2 are interpolated from the interpolation domain shown in Figure 2. In the present algorithm, the velocity components are collocated at a velocity node so that the same momentum control volume can be employed for both momentum equations.

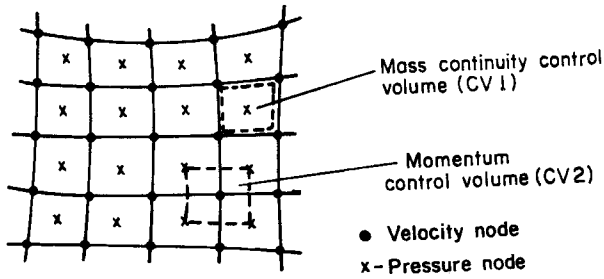

Figure 1. Schematic representation of grid discretization

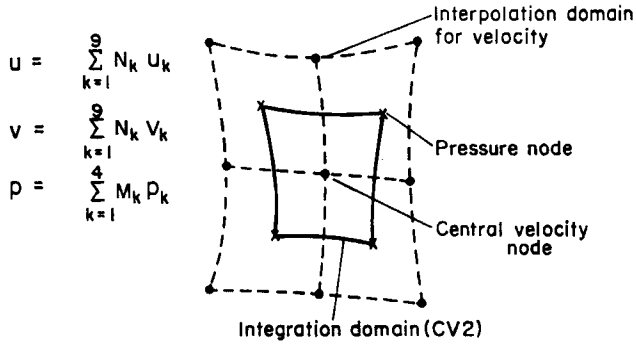

Figure 2. Interpolation domain for momentum balance

For mass balance on CV1,

$$\oint_{CS1} \mathbf{V}\cdot\hat{n}\,dl=\oint_{CS1}(un_x+vn_y)\,dl=0. \tag{1}$$

Here **V** is the velocity vector and dl is the elemental length along the boundary (CS1) of the control volume; u and v are the Cartesian velocity components. The direction cosines of the outward normal ($\hat{n}$) on the boundary are n_x and n_y, respectively.

For momentum balance on CV2,

x momentum

$$\rho\left\{\frac{\partial}{\partial t}\int\int_{CV2} u\,dA+\oint_{CS2} u(un_x+vn_y)\,dl\right\}=\oint_{CS2}\left\{-pn_x+2\mu\frac{\partial u}{\partial x}n_x+\mu\left(\frac{\partial u}{\partial y}+\frac{\partial v}{\partial x}\right)n_y\right\}dl, \tag{2}$$

y momentum

$$\rho\left\{\frac{\partial}{\partial t}\int\int_{CV2} v\,dA+\oint_{CS2} v(un_x+vn_y)\,dl\right\}=\oint_{CS2}\left\{-pn_y+2\mu\frac{\partial v}{\partial y}n_y+\mu\left(\frac{\partial u}{\partial y}+\frac{\partial v}{\partial x}\right)n_x\right\}dl, \tag{3}$$

where p is the non-gravitational pressure, ρ is the density and μ is the dynamic viscosity.

2.2. *Interpolation of flow variables within respective control volumes*

Since the order of momentum equations is higher than of the continuity equation, velocity

variables have been interpolated using biquadratic and bilinear functions for momentum and mass balances, respectively.

Thus, for the continuity equation

$$u=\sum_{i=1}^{4} M_i u_i, \qquad v=\sum_{i=1}^{4} M_i v_i \tag{4}$$

and for momentum equations

$$u=\sum_{i=1}^{9} N_i u_i, \qquad v=\sum_{i=1}^{9} N_i v_i, \tag{5}$$

where u_i, v_i are the nodal velocities for the respective control volumes. Also M_i, N_i are the linear and quadratic Lagrangian interpolation functions,[15] respectively. The variation of pressure over the momentum control volume is similarly expressed in the form

$$p=\sum_{i=1}^{4} M_i p_i. \tag{6}$$

The number of continuity cells (or equations) has to match exactly with the number of pressure variables, since mass imbalance in each continuity cell is used for pressure correction. It is for this reason that the pressures have been placed at the centroids of the continuity control volumes. The transient terms of the momentum equations are evaluated using the lumping concept:

$$\rho\frac{\partial}{\partial t}\iint_{CV2} u\,\mathrm{d}A=\rho A_{CV2}\dot{u}, \qquad \rho\frac{\partial}{\partial t}\iint_{CV2} v\,\mathrm{d}A=\rho A_{CV2}\dot{v}, \tag{7}$$

where A_{CV2} is the area of the control volume CV2 and $\dot{u}, \dot{v}$ are the time derivatives of the velocity components at the central node.

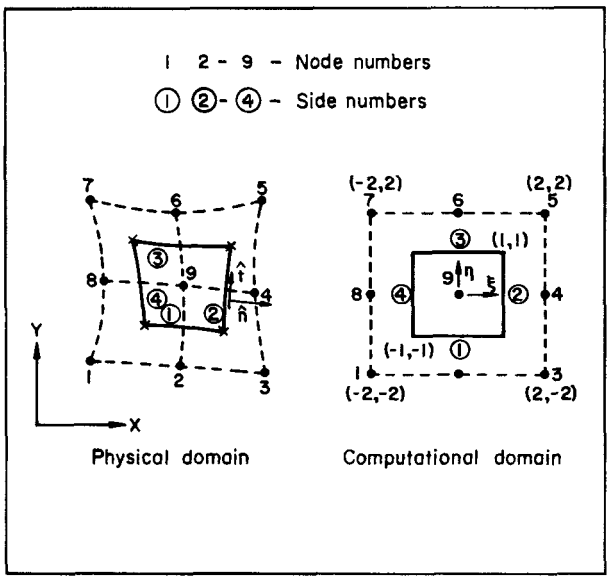

Figure 3. Transformation of a curvilinear control volume into a square computational cell

2.3. Numerical evaluation of the area and line integrals

In equations (2) and (3), integrations are carried out by Gauss–Legendre quadrature. Isoparametric mapping (Figure 3) is employed for transforming the cell geometry into a square computational cell for performing numerical quadrature. The co-ordinates are thus interpolated as

$$x=\sum_{i=1}^{9} N_i x_i, \qquad y=\sum_{i=1}^{9} N_i y_i, \tag{8}$$

where (x_i, y_i) are the co-ordinates of the nodes surrounding the control volume as shown in Figure 3.

It is necessary that the arc lengths, areas, surface integrals, derivatives and line integrals in the physical co-ordinate system be converted to the computational co-ordinates ξ and η. Applying the chain rule,

$$\begin{bmatrix} dx \\ dy \end{bmatrix} = \begin{bmatrix} \frac{\partial x}{\partial \xi} & \frac{\partial x}{\partial \eta} \\ \frac{\partial y}{\partial \xi} & \frac{\partial y}{\partial \eta} \end{bmatrix} \begin{bmatrix} d\xi \\ d\eta \end{bmatrix} = \begin{bmatrix} \sum_{i=1}^{9} \frac{\partial N_i}{\partial \xi} x_i & \sum_{i=1}^{9} \frac{\partial N_i}{\partial \eta} x_i \\ \sum_{i=1}^{9} \frac{\partial N_i}{\partial \xi} y_i & \sum_{i=1}^{9} \frac{\partial N_i}{\partial \eta} y_i \end{bmatrix} \begin{bmatrix} d\xi \\ d\eta \end{bmatrix} . \tag{9}$$

The derivatives are obtained as

$$\begin{bmatrix} \frac{\partial \phi}{\partial x} \\ \frac{\partial \phi}{\partial y} \end{bmatrix} = [J]^{-1} \begin{bmatrix} \frac{\partial \phi}{\partial \xi} \\ \frac{\partial \phi}{\partial \eta} \end{bmatrix} = [J]^{-1} \begin{bmatrix} \frac{\partial N_1}{\partial \xi} & \frac{\partial N_2}{\partial \xi} & \cdots & \frac{\partial N_9}{\partial \xi} \\ \frac{\partial N_1}{\partial \eta} & \frac{\partial N_2}{\partial \eta} & & \frac{\partial N_9}{\partial \eta} \end{bmatrix} \begin{bmatrix} \phi_1 \\ \phi_2 \\ \vdots \\ \phi_9 \end{bmatrix} , \tag{10}$$

where ϕ can be u or v and J is the Jacobian of transformation.

On the rth side ($r=1,2,3,4$) the elemental length vector dl_r (defined according to the anticlockwise sense of integration) can be written as

$$dl_r = dx_r \hat{i} + dy_r \hat{j} = \left\{ \left(\frac{\partial x}{\partial \xi}\right)_r d\xi + \left(\frac{\partial x}{\partial \eta}\right)_r d\eta \right\} \hat{i} + \left\{ \left(\frac{\partial y}{\partial \xi}\right)_r d\xi + \left(\frac{\partial y}{\partial \eta}\right)_r d\eta \right\} \hat{j} . \tag{11}$$

The outward unit normal vectors on corresponding cell boundaries are given by

$$\hat{n}_r = \left\{ \frac{\left(\frac{\partial y}{\partial \zeta}\right)_r \hat{i} - \left(\frac{\partial x}{\partial \zeta}\right)_r \hat{j}}{\left(\frac{\partial l}{\partial \zeta}\right)_r} \right\} \cdot (-1)^m , \tag{12}$$

where $m=0$ for $r=1,2$; $m=1$ for $r=3,4$ and

$$\left(\frac{dl}{d\zeta}\right)_r = \sqrt{\left\{ \left(\frac{\partial x}{\partial \zeta}\right)_r^2 + \left(\frac{\partial y}{\partial \zeta}\right)_r^2 \right\}},$$

$\zeta=\xi$ for $r=1,3$ and $\zeta=\eta$ for $r=2,4$. Also, the elemental length, dl is represented as

$$dl = \left(\frac{\partial l}{\partial \xi}\right)_r d\xi \quad \text{as } \eta = \text{constant for } r=1 \text{ and } 3$$

and

$$dl=\left(\frac{\partial l}{\partial \eta}\right)_r d\eta \quad \text{as } \xi=\text{constant for } r=2 \text{ and } 4.$$

Lastly, the elemental area, dA, is expressed as

$$dA=|J|\,d\xi\,d\eta. \tag{13}$$

Now all the integrals appearing in equations (2) and (3) can be rewritten in terms of ξ and η. Finally, these integrals are evaluated using 3-point Gauss–Legendre quadrature. During the application of this quadrature, the integrands are evaluated at each Gauss point of the respective boundary or control volume and all such Gauss point contributions are summed up.

For the continuity equation (1), it is not necessary to employ the numerical quadrature since the shape of CV1 is simpler and the velocity interpolation is linear. The procedure for deriving the pressure correction equation using equation (1) is described in a subsequent section.

2.4. *Matrix equations for momentum and mass balance*

The final discretized momentum equations for a velocity node in matrix form are

$$\underset{2\times 1}{\begin{Bmatrix}\dot{u}\\ \dot{v}\end{Bmatrix}}=\underset{2\times 18}{[\mathbf{CM}+\mathbf{DM}]}\underset{18\times 1}{\begin{Bmatrix}\mathbf{u}\\ \mathbf{v}\end{Bmatrix}}+\underset{2\times 4}{[\mathbf{SM}]}\underset{4\times 1}{\{\mathbf{p}\}}, \tag{14}$$

where **CM** and **DM** are coefficient submatrices representing the convective and diffusive contributions, respectively, and **SM** is the pressure coefficient matrix. Also **u**, **v** and **p** are vectors of nodal velocities and pressures corresponding to the momentum control volume under consideration.

The convective coefficient matrix [**CM**] can be expressed as

$$\underset{2\times 18}{[\mathbf{CM}]}=\left[\begin{array}{c:c}\underset{1\times 9}{\mathbf{CM}_1} & \underset{1\times 9}{\mathbf{0}}\\ \hdashline \mathbf{0} & \mathbf{CM}_2\end{array}\right], \tag{15a}$$

where the entries of the submatrices $\mathbf{CM}_1$ and $\mathbf{CM}_2$ are given by

$$\mathrm{CM}_{1j}=\mathrm{CM}_{2j}=\oint_{\mathrm{CS2}}\frac{1}{\rho A_{\mathrm{CV2}}}N_j(un_x+vn_y)\,dl \quad \text{for } j=1,\ldots 9. \tag{15b}$$

Applying Gauss–Legendre quadrature over each side of the control volume, the above expression is evaluated as

$$\mathrm{CM}_{1j}=\mathrm{CM}_{2j}=\frac{1}{\rho A_{\mathrm{CV2}}}\sum_{r=1}^{4}\sum_{k=1}^{3}\left[N_j\sum_{q=1}^{9}(u_qn_x+v_qn_y)N_q\right]w_k\Delta l_r, \tag{15c}$$

where

$$A_{\mathrm{CV2}}=\sum_{l=1}^{3}\sum_{k=1}^{3}|J|w_kw_l.$$

The corresponding diffusion matrix [**DM**] is expressed as

$$\underset{2\times 18}{[\mathbf{DM}]}=\left[\begin{array}{c:c}\underset{1\times 9\text{ each}}{\mathbf{DU}_1} & \mathbf{DV}_1\\ \hdashline \mathbf{DU}_2 & \mathbf{DV}_2\end{array}\right], \tag{16a}$$

where the entries of the submatrices $\mathbf{DU}_1, \mathbf{DV}_1, \mathbf{DU}_2$ and $\mathbf{DV}_2$ are

$$\mathrm{DU}_{1j}=\frac{1}{\rho A_{\mathrm{CV2}}}\sum_{r=1}^{4}\sum_{k=1}^{3}\left[2\mu n_x\frac{\partial N_j}{\partial x}+\mu n_y\frac{\partial N_j}{\partial y}\right]w_k\Delta l_r$$

$$\mathrm{DV}_{1j}=\frac{1}{\rho A_{\mathrm{CV2}}}\sum_{r=1}^{4}\sum_{k=1}^{3}\left[\mu n_y\frac{\partial N_j}{\partial x}\right]w_k\Delta l_r$$

$$\mathrm{DU}_{2j}=\frac{1}{\rho A_{\mathrm{CV2}}}\sum_{r=1}^{4}\sum_{k=1}^{3}\left[\mu n_x\frac{\partial N_j}{\partial y}\right]w_k\Delta l_r$$

$$\mathrm{DV}_{2j}=\frac{1}{\rho A_{\mathrm{CV2}}}\sum_{r=1}^{4}\sum_{k=1}^{3}\left[\mu n_x\frac{\partial N_j}{\partial x}+2\mu n_y\frac{\partial N_j}{\partial y}\right]w_k\Delta l_r \quad \text{for } j=1,\ldots,9. \tag{16b}$$

The pressure matrix in turn is

$$[\mathbf{SM}]=\underset{2\times 4}{\begin{bmatrix}\mathbf{SM}_1\\ \mathbf{SM}_2\end{bmatrix}}, \qquad \underset{1\times 4 \text{ each}}{} \tag{17a}$$

where the entries of the submatrices $\mathbf{SM}_1$ and $\mathbf{SM}_2$ are given by

$$\mathrm{SM}_{1j}=-\frac{1}{\rho A_{\mathrm{CV2}}}\sum_{r=1}^{4}\sum_{k=1}^{3}(M_j n_x)w_k\Delta l_r$$

$$\mathrm{SM}_{2j}=-\frac{1}{\rho A_{\mathrm{CV2}}}\sum_{r=1}^{4}\sum_{k=1}^{3}(M_j n_y)w_k\Delta l_r \quad \text{for } j=1,\ldots,4. \tag{17b}$$

On account of linear interpolation for the velocity variable within the continuity control volume CV1, the discretized form of mass balance equation becomes

$$\sum_{r=1}^{4}(\bar{u}_r n_{xr}+\bar{v}_r n_{yr})\Delta l_r=0, \tag{18}$$

where $\bar{u}_r, \bar{v}_r$ are, respectively, the average values of x and y velocity components on the sides of CS1.

2.5. Upwinding of convection terms

In the numerical solution of Navier–Stokes equations, the convection terms need specific attention for conserving the transportive property. The present algorithm produces trouble-free solutions up to a cell Reynolds number of about 6. Spatially, oscillatory velocity fields result for higher cell Reynolds numbers which may be attributed to the need for upwinding.

An effective upwind discretization for the convection terms is implemented by setting

$$\mathrm{CM}_{1j}u_j=\mathrm{CM}_{2j}u_j=\frac{1}{\rho A_{\mathrm{CV2}}}\oint(un_x+vn_y)G_j u_j\,\mathrm{d}l, \tag{19}$$

where G_j is the upwind basis function given by

$$\sum_{j=1}^{9}G_j u_j=\sum_{j=1}^{9}(1-\alpha)N_j u_j+\alpha u_{\mathrm{b}}. \tag{20}$$

The subscript 'b' corresponds to the node situated upstream of the concerned face and α is a fraction; for purely symmetric parabolic interpolation $\alpha=0$ and for first-order upwind interpolation, $\alpha=1$.

2.6. Derivation of pressure correction equation

When the time gradient of velocities is expressed in discretized form, equation (14) becomes

$$\begin{Bmatrix} u^{n+1} \\ v^{n+1} \end{Bmatrix} = \begin{Bmatrix} u^n \\ v^n \end{Bmatrix} + \Delta t[\mathbf{CM}^n + \mathbf{DM}] \begin{Bmatrix} \mathbf{u}^n \\ \mathbf{v}^n \end{Bmatrix} + \Delta t[\mathbf{SM}]\{\mathbf{p}\}^{n+1}, \tag{21}$$

where the superscripts n and $n+1$ denote time levels. However, at the start of calculation for each time step, $\mathbf{p}^{n+1}$ is not known and hence equation (14) predicts provisional velocities (represented by a superscript asterisk) that satisfy momentum balance corresponding to the $\mathbf{p}^n$ pressures. When both pressure and velocities undergo iterative corrections, $\mathbf{p}^n$ takes up provisional value $\mathbf{p}^*$. Thus,

$$\begin{Bmatrix} \mathbf{u}^* \\ \mathbf{v}^* \end{Bmatrix} = \begin{Bmatrix} u^n \\ v^n \end{Bmatrix} + \Delta t[\mathbf{CM}^n + \mathbf{DM}] \begin{Bmatrix} \mathbf{u}^n \\ \mathbf{v}^n \end{Bmatrix} + \Delta t[\mathbf{SM}]\{\mathbf{p}^*\}. \tag{22}$$

As continuity equation is satisfied in each cell, all provisional velocities reach the final values for the present time step $(n+1)$. Subtracting equation (22) from equation (21) the expressions for the velocity corrections can be obtained as

$$\underset{2\times 1}{\begin{Bmatrix} u^{n+1} - u^* \\ v^{n+1} - v^* \end{Bmatrix}} = \underset{2\times 1}{\begin{Bmatrix} \delta u \\ \delta v \end{Bmatrix}} = \Delta t \underset{2\times 4}{[\mathbf{SM}]} \underset{4\times 1}{\{\delta \mathbf{p}\}}, \tag{23}$$

where δv, δv and $\delta \mathbf{p}$ are the velocity and pressure corrections. Applying the principle of continuity at $(n+1)$th level,

$$\sum_{r=1}^{4} (\bar{u}_r^{n+1} n_{xr} + \bar{v}_r^{n+1} n_{yr}) \Delta l_r = 0. \tag{24a}$$

The unconverged velocities, however, do not satisfy the continuity equation, leading to a non-zero residue of the form

$$\sum_{r=1}^{4} (\bar{u}_r^* n_{xr} + \bar{v}_r^* n_{yr}) \Delta l_r = R. \tag{24b}$$

Subtracting equation (24b) from equation (24a), we obtain

$$\sum_{r=1}^{4} (\delta \bar{u}_r n_{xr} + \delta \bar{v}_r n_{yr}) \Delta l_r = -R, \tag{25}$$

where $\delta \bar{u}_r$ and $\delta \bar{v}_r$ are the average velocity corrections on the rth side, so as to satisfy continuity principle in the control volume. The quantities $\delta \bar{u}_r$ and $\delta \bar{v}_r$ are expressed in terms of the nodal velocity corrections, which in turn are substituted by proper pressure correction terms using equation (23). These average velocity corrections, when evaluated as the simple average of the corresponding nodal velocities, lead to decoupling of pressure in alternate continuity cells. Similar pressure splitting has also been observed by Majumdar *et al.*[18]

Introducing face-centre velocity corrections $\delta u_{\mathrm{f},r}$ and $\delta v_{\mathrm{f},r}$ (Figure 4), the average corrections on the east side of CV1 can be expressed as

$$\begin{aligned} \delta \bar{u}_{\mathrm{e}} &= \tfrac{1}{6}\delta u_{\mathrm{II}} + \tfrac{1}{6}\delta u_{\mathrm{III}} + \tfrac{2}{3}\delta u_{\mathrm{f,e}}, \\ \delta \bar{v}_{\mathrm{e}} &= \tfrac{1}{6}\delta v_{\mathrm{II}} + \tfrac{1}{6}\delta v_{\mathrm{III}} + \tfrac{2}{3}\delta v_{\mathrm{f,e}}, \end{aligned} \tag{26}$$

where II and III are the velocity nodes lying on the east face. Similarly, the average corrections on other sides can also be estimated. Note that equation (26) amounts to the application of

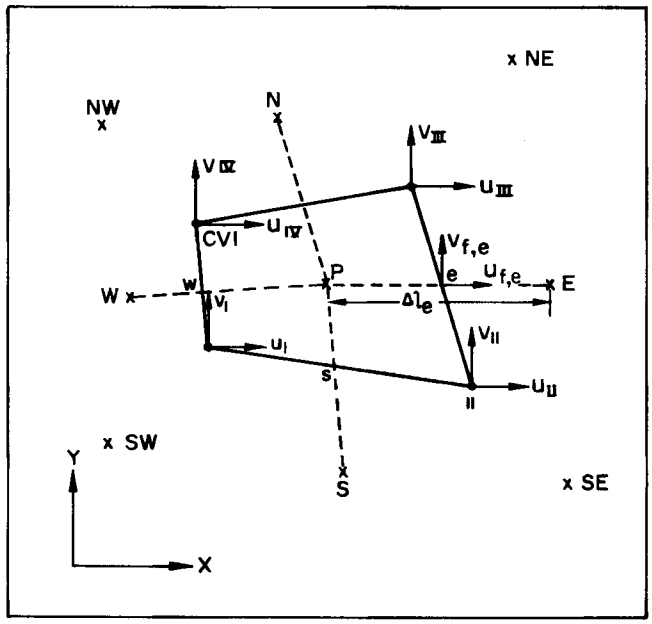

Figure 4. Pressure velocity coupling in a continuity control volume

Simpson's rule along the boundaries of CV1. In order to find the expressions for $\delta u_{f,r}$ and $\delta v_{f,r}$, a modified form of equation (23) can be written for the velocity correction vector as

$$\delta \mathbf{V} = -\frac{\Delta t}{\rho}\nabla(\delta p). \tag{27}$$

Eventually, we can write

$$\delta u_{f,e} = (\hat{i}\cdot\delta\mathbf{V})_{f,e} = -\frac{\Delta t}{\rho}\hat{i}\cdot\left\{\hat{e}\frac{\delta p_E - \delta p_P}{\Delta l_E}\right\}$$

or

$$\delta u_{f,e} = \frac{\Delta t}{\rho}\left\{\frac{x_E - x_P}{\Delta l_E}\right\}\left\{\frac{\delta p_P - \delta p_E}{\Delta l_E}\right\}. \tag{28a}$$

Similarly,

$$\delta v_{f,e} = \frac{\Delta t}{\rho}\left\{\frac{y_E - y_P}{\Delta l_E}\right\}\left\{\frac{\delta p_P - \delta p_E}{\Delta l_E}\right\}. \tag{28b}$$

Here $\hat{e}$ is the unit vector connecting the central pressure node P to the eastern neighbouring pressure node E. Also, Δl_E is the distance between the nodes P and E. Similarly, the other face-centre velocity corrections can be obtained as

$$\delta u_{f,(n,w,s)} = \frac{\Delta t}{\rho}\frac{(x_{(N,W,S)} - x_P)}{\Delta l_{(N,W,S)}}\left\{\frac{\delta p_P - \delta p_{(N,W,S)}}{\Delta l_{(N,W,S)}}\right\}, \tag{29a}$$

$$\delta v_{f,(n,w,s)} = \frac{\Delta t}{\rho} \frac{(y_{(N,W,S)} - y_P)}{\Delta l_{(N,W,S)}} \left\{ \frac{\delta p_P - \delta p_{(N,W,S)}}{\Delta l_{(N,W,S)}} \right\}, \tag{29b}$$

where the lower-case subscripts (n, w, s) refer to the corresponding boundary faces, while the upper-case subscripts (N, W, S) refer to the pressure nodes of the corresponding continuity cells. The mass residue contribution R_e to the east face is given by

$$\Delta l_e(\delta \bar{u}_e n_{xe} + \delta \bar{v}_e n_{ye}) = -R_e. \tag{30a}$$

Substituting for $\delta \bar{u}_e$ and $\delta \bar{v}_e$ from equation (26), we have

$$\Delta l_e\{\tfrac{1}{6}\delta u_{II} + \tfrac{1}{6}\delta u_{III} + \tfrac{2}{3}\delta u_{f,e}\} n_{xe} + \Delta l_e\{\tfrac{1}{6}\delta v_{II} + \tfrac{1}{6}\delta v_{III} + \tfrac{2}{3}\delta v_{f,e}\} n_{ye} = -R_e. \tag{30b}$$

From equation (23), the nodal velocity corrections are given by

$$\begin{Bmatrix} \delta u_{II} \\ \delta v_{II} \end{Bmatrix} = \Delta t [\mathbf{SM}]_{II} \{\delta p_S \; \delta p_{SE} \; \delta p_E \; \delta p_P\}^T \tag{31a}$$

and

$$\begin{Bmatrix} \delta u_{III} \\ \delta v_{III} \end{Bmatrix} = \Delta t [\mathbf{SM}]_{III} \{\delta p_N \; \delta p_{NE} \; \delta p_E \; \delta p_P\}^T. \tag{31b}$$

It is to be noted that in equations (31a) and (31b), the pressure coefficient matrix **SM** is evaluated at nodes II and III. After substituting equations (28a), (28b), (31a) and (31b) into equation (30b), the residue contribution of the east face R_e can be calculated in terms of pressure corrections. Similar exercise for the other sides of the continuity cells would lead to a pressure correction equation of the form

$$\underset{1\times 9}{[\mathbf{CP}]} \underset{9\times 1}{\{\delta \mathbf{P}\}} = -R, \tag{32}$$

where **CP** is the coefficient matrix corresponding to the pressure correction array and R is the mass residue arising from the velocities updated by momentum equations. For later iterations, the incremental residue is used in equation (32) which is calculated from equation (25). Equation (32) has a strong diagonal dominance ensuring smooth convergence with respect to iterations. In the present work, point-by-point iteration with successive overrelaxation has been employed to solve the pressure correction equations in the whole domain. The pressure and velocity corrections are iteratively improved until the corrections to the mass residues decrease below a predefined convergence level (10^{-7}) for all the continuity cells. Thus, by explicit momentum evaluation and implicit satisfaction of continuity, time marching of nodal velocities and pressures are continued until steady state is reached from the given initial conditions.

3. TEST PROBLEMS

The EXTRA-FLAG algorithm is first tested on some simple two-dimensional flow situations in orthogonal configurations, namely, the lid-driven square cavity flow and the developing flow in a rectangular channel. Subsequently, flow in another orthogonal geometry with more complex physics has been solved – the flow over square cylinder placed in a channel. Next the algorithm has been successfully applied to a simple non-orthogonal geometry – the lid-driven oblique cavity. Finally, the flow over a circular cylinder placed in a channel has been solved with non-orthogonal mesh.

3.1. *Lid-driven square cavity*

The numerical domain consists of a two-dimensional lid-driven square cavity with no-slip and impervious boundary conditions at the bottom and side walls, except at the top surface where the u velocity is constant and equal to ULID. In the governing equations, the velocities have been non-dimensionalized with respect to the cavity height H and the Reynolds number is defined as $Re = (\text{ULID} \cdot H)/\nu$. The streamline patterns using 81×81 grid for the aforesaid two-dimensional cavity at $Re = 400$ are shown in Figure 5. These compare favourably with the numerical solution of Ghia *et al.*[19] In Figure 6, u velocity components at the vertical mid-plane are plotted for 41×41 and 81×81 grids. These are also compared with the results obtained by Ghia *et al.*[19] and Peyret and Taylor.[20] It may be mentioned that Ghia *et al.* adopted a 129×129 mesh with multigrid technique. However, present computations on 81×81 grid show good agreement with the results of Ghia *et al.* as seen in Figure 6. The minimum u velocity position and the variation of u velocity match well.

For a Reynolds number 1000, the extreme values of velocities have been predicted with a 41×41 grid. These are compared with the results obtained by Ghia *et al.*[19] and Wang *et al.*[21] in Table I. The discrepancy between the results of Ghia *et al.*[19] and those of ours can be attributed to the comparatively coarser grid employed in the present work. However, as compared to the predictions of Wang *et al.*[21] which were obtained on a still coarser grid, the present results are better, as expected.

3.2. *Developing flow in a channel*

Developing flow in a rectangular channel has been simulated in an effort to check the ability of the algorithm to predict the hydrodynamic entrance length in a two-dimensional channel flow. In the governing equations, the velocities are non-dimensionalized with respect to the average incoming velocity U_{av} at the channel inlet. All lengths have been non-dimensionalized with

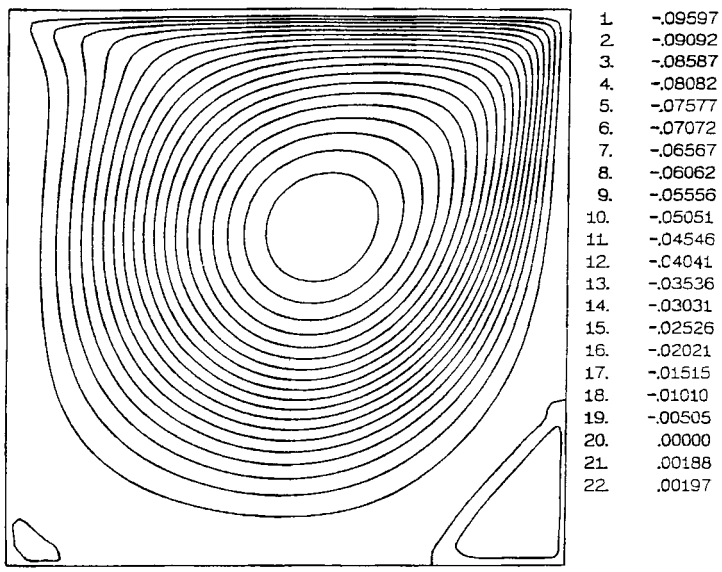

Figure 5. Streamlines in a lid-driven square cavity for $Re = 400$ (81×81 grid)

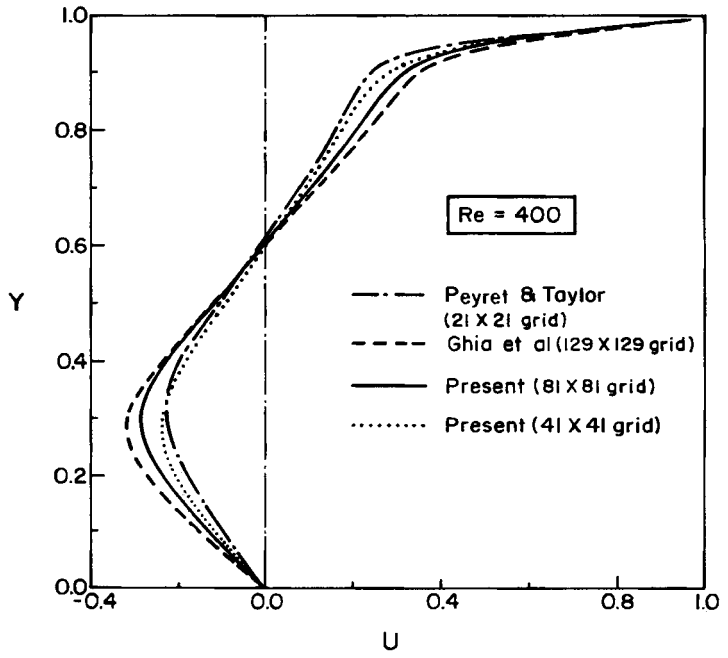

Figure 6. Variation of U velocity along the vertical mid-plane for the lid-driven flow in a square cavity

Table I. Extremes in velocity for the driven cavity, $Re = 1000$

Authors	u_{min} at $x=0{\cdot}5$		v_{min} at $y=0{\cdot}5$		v_{max} at $y=0{\cdot}5$	
	u_{min}	y	v_{min}	x	v_{max}	x
Ghia *et al.*[19] 129 × 129 grid	−0·388	0·172	−0·516	0·906	0·371	0·156
Wang *et al.*[21] 21 × 21 grid	−0·135	0·240	−0·300	0·930	0·138	0·041
Present 41 × 41 grid	−0·244	0·175	−0·361	0·925	0·227	0·187

respect to the channel height H and the Reynolds number is defined as $Re=(U_{av}H)/\nu$. No-slip and impervious boundary conditions for velocities are applied on the top and the bottom walls ($u=0$, $v=0$). At the inlet, the normal component of velocity is zero ($v=0$) and a uniform axial velocity profile ($u=U_{av}$) is deployed. At the exit of the channel, second derivatives of the dependent variables in the flow direction are set equal to zero ($\partial^2 u/\partial x^2=\partial^2 v/\partial x^2=0$) in order to ensure smooth transition through the outflow boundary. The computed velocity profile corroborates well with the results of Abarbanel *et al.*[22]

Distributions of skin friction ($C_f Re$) along the channel walls are exactly same for the top and bottom walls. As expected, the skin friction values ($C_f Re$) for all Reynolds numbers asymptotically reach a constant value of 12 (which is the value corresponding to the fully developed

Poiseuille flow) from very high values near the inlet (Figure 7). However, from our results, it is quite evident that the entry length (the length at which fully developed velocity profile culminates) is a function of Reynolds number and this functional relationship may be summarized as $(x/H) \approx 0{\cdot}055 Re$. Defining the fully developed condition as the attainment of 99% of Poiseuille profile, our prediction of the entry length corroborates the results available in literature (see Reference 23).

3.3. Flow over square cylinder placed in a rectangular channel

The flow physics and the finer details of this problem are well discussed in authors' earlier work using MAC algorithm.[24] Here this problem has been chosen to establish the applicability of EXTRA-FLAG by repeating similar calculations. The geometry of the problem is shown in Figure 8. A fully developed flow field is considered at the channel inlet. On the cyliner no-slip and impervious conditions are prescribed. The other boundary conditions at the channel walls and exit sections are the same as in the developing channel flow problem discussed earlier.

The first critical Reynolds number for the inception of wake oscillation is around 90 for a cylinder to channel height ratio of 0·25 (Figure 9). With the MAC algorithm, the corresponding value of the Reynolds number was found to be 85.[25] Davis *et al.*[25] found the same as ≈ 100 and Okajima[26] reported this Reynolds number as 70 for flows over rectangular cylinders placed in an infinite medium. Also, the formation of von Karman vortex street and shedding frequency match very well with the earlier work.[24] The alternate shedding of vortices are quite well captured in the streamline plots for $Re_B = 500$ (Figure 10). However, the present algorithm being in its developmental stage, the computer code is not properly optimized and it does not fully exploit the features of orthogonal geometry. Thus, it takes relatively more execution time than the corresponding MAC code (see the appendix). In order to establish the potential utility of the present

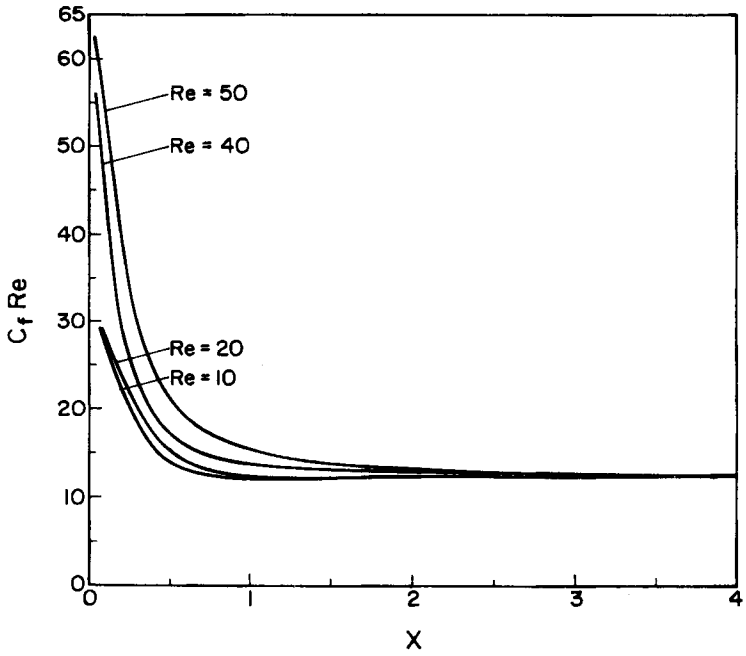

Figure 7. Variation of $C_f Re$ in a two-dimensional channel

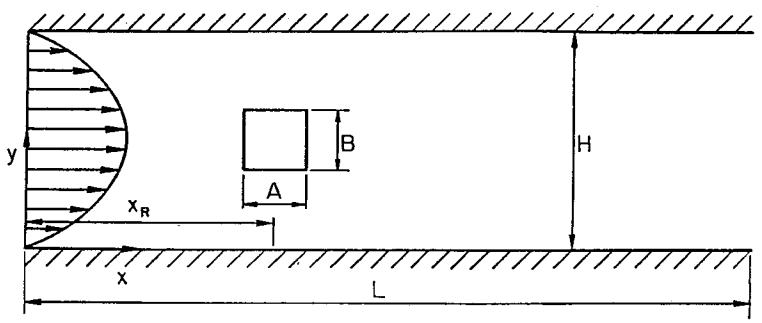

Figure 8. Flow in a rectangular channel with built-in square cylinder

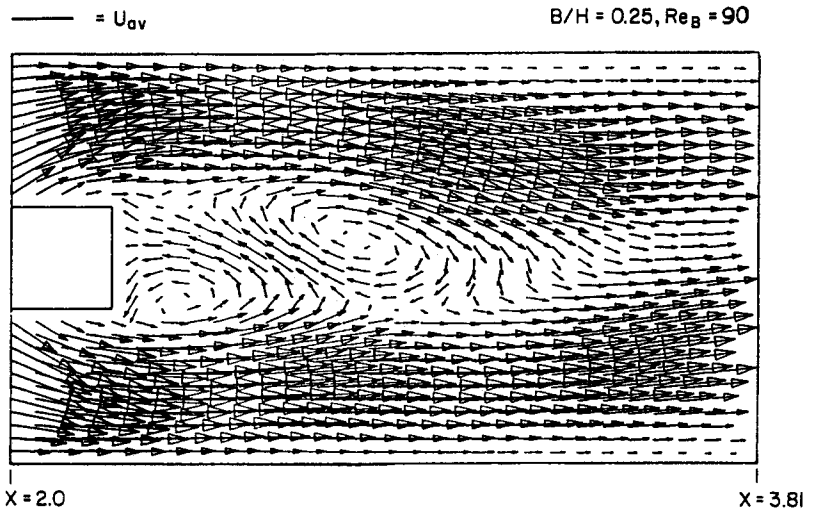

Figure 9. Asymmetry in the wake behind the square cylinder

algorithm to non-orthogonal curvilinear geometries, two related problems are discussed in the following sections.

3.4. Lid-driven oblique cavity

The geometry of the cavity is such that its slant height, base and lid dimensions are all equal and the slant angle for the sides is 60°. A non-orthogonal grid is necessary for this geometry. The boundary conditions are same as those of the lid-driven square cavity problem. Cartesian velocity components have been used in the numerical simulation.

On a 21 × 21 grid, this problem has been solved corresponding to the Reynolds numbers of 100, 400 and 1000. Figure 11 shows the velocity vectors for $Re = 1000$. The vortex centre in oblique cavity shifts with Reynolds number similar to the trend seen for the square cavity. The u-velocity distributions along the slant mid-plane (Figure 12) show physically meaningful values and minimum u velocity positions for different Reynolds numbers. It is noted that our results for oblique cavity compare favourably with the results of Peric.[27] Due to sparse numerical or experimental database on oblique cavity, rigorous comparison was not possible.

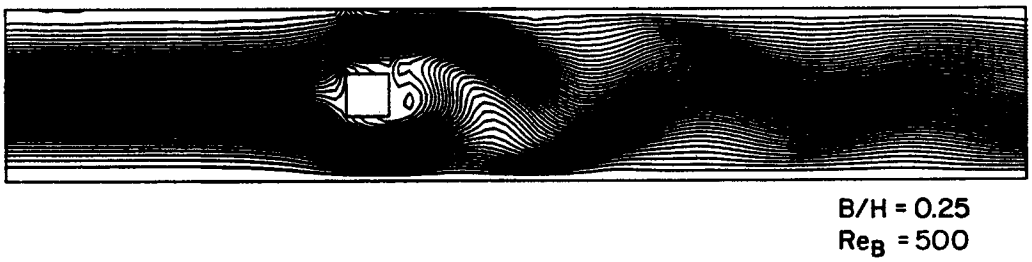

Figure 10. Streamlines in a channel with built-in square cylinder at $Re_B = 500$

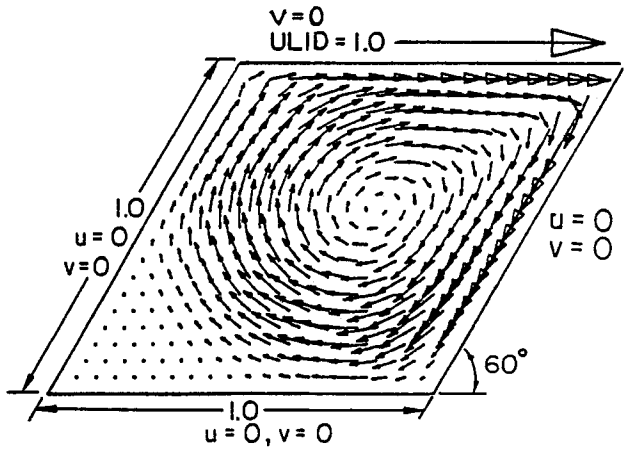

Figure 11. Velocity vectors in a lid-driven oblique cavity for $Re = 1000$

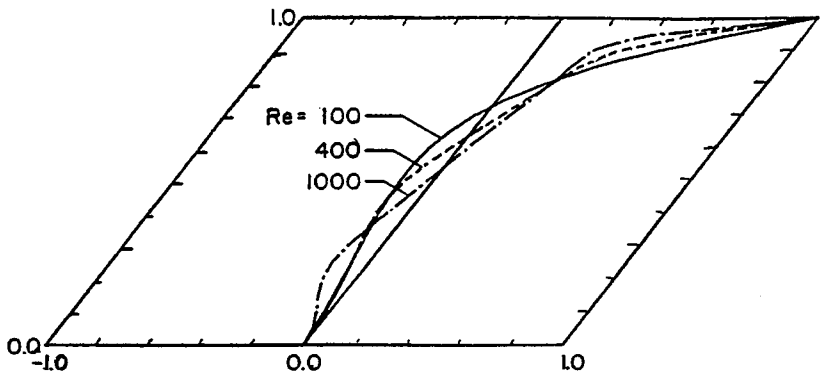

Figure 12. Variation of U velocity along the mid-plane in an oblique cavity

3.5. Flow over circular cylinder placed in a rectangular channel

Study of vortex structure behind a circular cylinder placed in a rectangular channel is an attractive exercise to establish the applicability of EXTRA-FLAG to a complex non-orthogonal geometry. A host of investigations[28-30] have been reported which explain the features of vortex shedding and the wakezone aerodynamics.

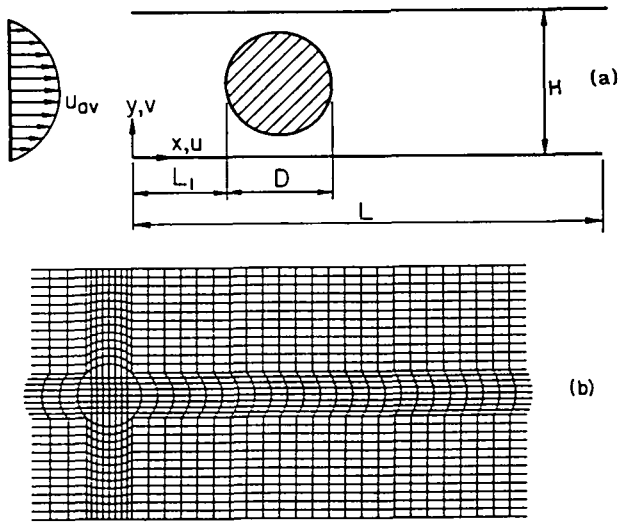

Figure 13. Configuration definition (a) and computational grid (b) for two-dimensional flow in a channel with built-in circular cylinder

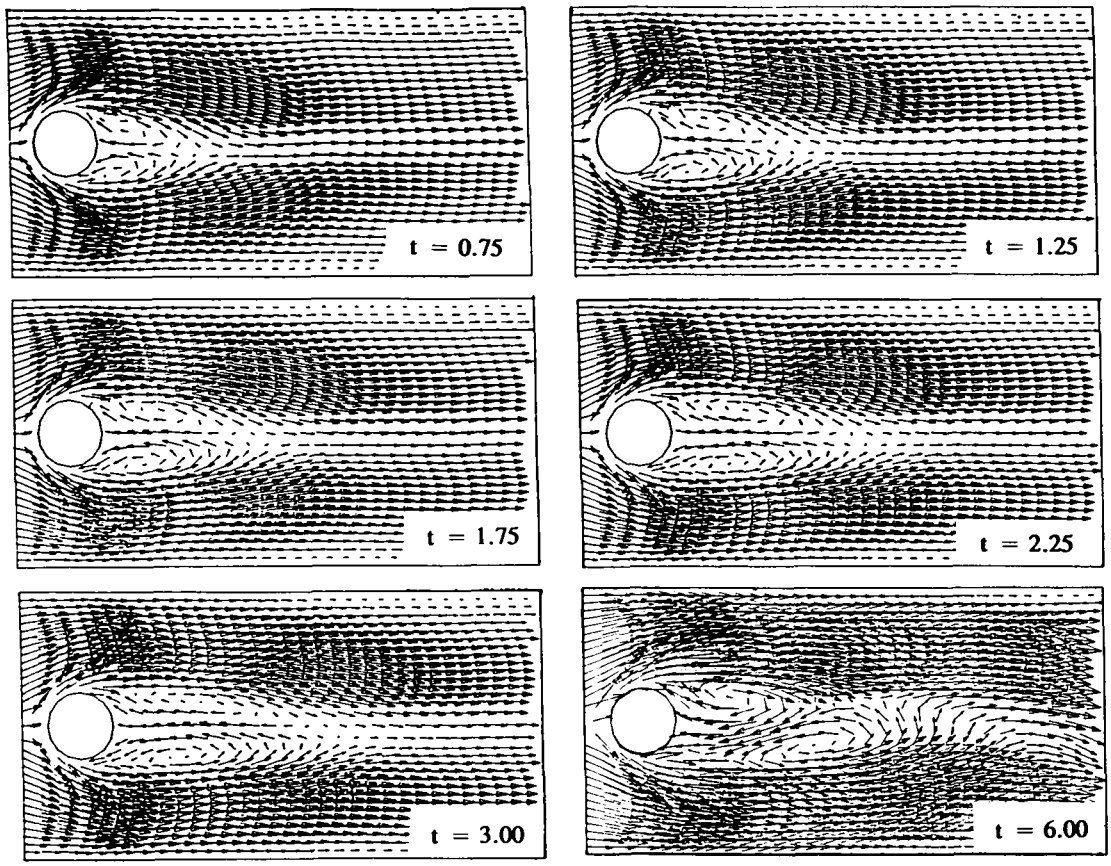

Figure 14. Time evolution of velocity for flow through a channel with built-in circular cylinder ($Re_D = 112$)

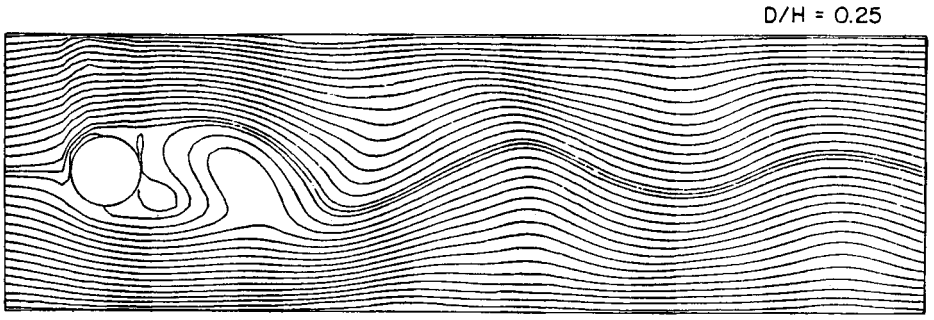

Figure 15. Streamlines in a channel with built-in circular cylinder at $Re_D = 625$

The flow domain resembles that for the square cylinder problem while the width (B) of the cylinder has been replaced by the diameter (D). The boundary conditions are also similar to the case of square cylinder. A non-orthogonal algebraically generated grid is used as shown in Figure 13. Unlike the conventional body-fitted co-ordinate system based solvers, EXTRA-FLAG does not need a smooth grid. Computations have been performed at Reynolds numbers (Re_D) of 87, 112 and 625 for the blockage ratio of 0·25. The initiation of vortex shedding occurred at $Re_D = 87$ with a Strouhal number of 0·2341. Figure 14 shows the time evolution of the velocity vectors for $Re_D = 112$. Corresponding to a non-dimensional time of 2·25, the flow has become periodic in the near-wake. At $t = 6·0$, the vector plot shows that periodicity has set in. For $Re_D = 625$, the stream function plot (Figure 15) shows the dominance of oscillations in the entire wake region.

4. CONCLUSION

The EXTRA-FLAG algorithm appears to have an excellent potential for predicting complex flows in non-orthogonal geometries. The accuracy of the predictions is comparable to those of the existing methods and the convergence characteristics of the continuity iterations are quite good. The method can easily be extended to three-dimensional flows also.

APPENDIX

Table II. Typical CPU times reqired on a CONVEX C-220 machine for different flow problems studied

No.	Problem	Grid	Time monitored for	CPU time (s)
1	Square cavity problem for $Re = 100$ (EXTRA-FLAG)	21 × 21	Steady-state	45·0
2	Square cavity problem for $Re = 1000$ (EXTRA-FLAG)	21 × 21	Steady-state	117·6
3	Oblique cavity problem for $Re = 1000$ (EXTRA-FLAG)	21 × 21	Steady-state	190·7
4	Developing flow in a channel for $Re = 40$ (EXTRA-FLAG)	21 × 11	Steady-state	30·1
5	Flow over square cylinder placed in a channel solved by EXTRA-FLAG for $Re = 450$	97 × 33	One time-step calculation after stabilization of periodicity	49·5

APPENDIX (Continued)

Table II. (Continued)

No.	Problem	Grid	Time monitored for	CPU time (s)
6	Flow over square cylinder placed in a channel solved by MAC method for $Re=450$	200×34	One time-step calculation after stabilization of periodicity	61·0
7	Flow over circular cylinder placed in a channel solved by EXTRA-FLAG for $Re=450$	97×33	One time-step calculation after stabilization of periodicity	74·3

REFERENCES

1. F. H. Harlow and J. E. Welch, 'Numerical calculation of time-dependant viscous incompressible flow of fluid with free surface', *Phys. Fluids*, **8**, 2182–2188 (1965).
2. F. H. Harlow and A. A. Amsden, 'The SMAC method: a numerical technique for calculating incompressible fluid flows', *Los Alamos Scientific Lab. Report LA 4370*, 1970.
3. A. J. Chorin, 'A numerical method for solving incompressible viscous flow problems', *J. Comput. Phys.*, **2**, 12–26 (1967).
4. C. W. Hirt and J. L. Cook, 'Calculating three-dimensional flows around structures and over rough terrain', *J. Comput. Phys.*, **10**, 324–340 (1972).
5. S. V. Patankar and D. B. Spalding, 'A calculation procedure for heat mass and momentum transfer in three-dimensional parabolic flows', *Int. J. Heat Mass Transfer*, **15**, 1787–1806 (1972).
6. S. V. Patankar, *Numerical Heat Transfer and Fluid Flow*, Hemisphere, Washington, DC, 1980.
7. S. V. Patankar, 'A calculation procedure for two-dimensional elliptic situations', *Numer. Heat Transfer*, **4**, 409–425 (1981).
8. J. P. Van Doormaal and G. D. Raithby, 'Enhancements of the SIMPLE method for predicting incompressible fluid flows', *Numer. Heat transfer*, **7**, 147–163 (1984).
9. J. F. Thompson, Z. U. A. Warsi and C. W. Mastin, 'Boundary fitted coordinate system for numerical solution of partial differential equations – a review', *J. Comput. Phys.*, **47**, 1–108 (1982).
10. S. P. Vanka, B. C. J. Chen and W. T. Sha, 'A semi-implicit calculation procedure for flows described in boundary fitted coordinate systems', *Numer. Heat Transfer*, **3**, 1–19 (1980).
11. G. D. Raithby, P. F. Galpin and J. P. Van Doormaal, 'Prediction of heat and fluid flow in complex geometries using general orthogonal coordinates', *Numer. Heat Transfer*, **9**, 125–142 (1986).
12. W. Shyy, S. S. Tong and S. M. Correa, 'Numerical recirculating flow calculation using a body-fitted coordinate system', *Numer. Heat Transfer*, **8**, 99–113 (1985).
13. M. Peric, 'A finite volume method for the prediction of three dimensional fluid flow in complex ducts', *Ph.D. Thesis*, University of London, 1985.
14. O. C. Zienkiewicz, *The Finite Element Method*, McGraw-Hill, New York, 1977.
15. C. Taylor and T. G. Hughes, *Finite Element Programming of the Navier–Stokes Equations*, Pineridge, Swansea, 1981.
16. B. R. Baliga and S. V. Patankar, 'A control volume finite element method for two dimensional fluid flow and heat transfer', *Numer. Heat Transfer*, **6**, 245–261 (1983).
17. C. Prakash and S. V. Patankar, 'A control volume finite element method for predicting flow and heat transfer in ducts of arbitrary cross-sections – Part I & II', *Numer. Heat Transfer*, **12**, 389–437 (1987).
18. S. Majumdar, W. Rodi and S. P. Vanka, 'On the use of non-staggered pressure velocity arrangement for numerical solution of incompressible flows', *Report SFB 210/T/35*, University of Karlsruhe, Germany, 1987.
19. U. Ghia, K. N. Ghia and C. T. Shin, 'High-resolutions for incompressible flow using the Navier–Stokes equations and a multigrid method', *J. Comput. Phys.*, **48**, 387–411 (1982).
20. R. Peyret and T. D. Taylor, *Computational Methods for Fluid Flow*, Springer, New York, 1983, pp. 199–207.
21. Y. Wang, J. He and B. Q. Zhang, 'A calculation procedure for steady two dimensional elliptic flows', *Int. j. numer. methods fluids*, **9**, 609–617 (1989).
22. S. Abarbanel, S. Bennett, A. Brandt and J. Gillis, 'Velocity profiles of flow at low Reynolds numbers', *J. appl. mech. ASME*, **37**, 2–4 (1970).
23. Y. L. Wang and P. A. Longwell, 'Laminar flow in the inlet section of parallel plates', *AIChEJ.*, **10**, 323 (1964).
24. A. Mukhopadhyay, G. Biswas and T. Sundararajan, 'Numerical investigation of confined wakes behind a square cylinder in a channel', *Int. j. numer. methods fluids*, **14**, 1473–1484 (1992).
25. R. W. Davis, E. F. Moore and L. P. Purtell, 'A numerical and experimental study of confined wakes around rectangular cylinders', *Phys. Fluids*, **27**, 46–59 (1984).

26. A. Okajima, 'Numerical simulation of flow around rectangular cylinders', *J. Wind Eng. Ind. Aerodynam.*, **33,** 171–180 (1990).
27. M. Peric, 'Efficient semi-implicitly solving algorithm for nine-diagonal coefficient matrix', *Numer. Heat Transfer*, **11,** 251–279 (1987).
28. C. C. S. Song and M. Yuan, 'Simulation of vortex shedding flow about a circular cylinder at high Reynolds numbers', *J. Fluids Eng. ASME*, **112,** 155–164 (1990).
29. M. Braza, P. Chassaing and H. Ha-Minh, 'Numerical study and physical analysis of the pressure and velocity fields in the near wake of a circular cylinder', *J. Fluid Mech.*, **165,** 79–130 (1986).
30. P. Kiehm, N. K. Mitra and M. Fiebig, 'Numerical investigation of two- and three-dimensional confined wakes behind a circular cylinder in a channel', *AIAA 24th Aerospace Sciences Meeting*, Reno, Nevada, *AIAA Paper – 86-0035*, 1986.